Check for updates

ADVANCED FUNCTIONAL MATERIALS
www.afm-journal.de

Design of Sodium Chalcohalide Solid Electrolytes with Mixed Anions for All-Solid-State Sodium-Ion Batteries

Zhi Liang Dong, Baiju Sourav, Yi Gan, Vinicius Martins, Xuchun Wang, Amirhosein Mozafarighoraba, Ruirui Zhang, Colin Turner, Xin Pang, Hamidreza Abdolvand, Yining Huang, Payam Kaghazchi, Tsun-Kong Sham,* and Yang Zhao**

Solid-state sodium-ion batteries (SSNIBs) have emerged as a promising alternative to lithium-ion systems for grid-scale energy storage, owing to sodium's abundance and the improved safety of solid-state designs. Among various solid-state electrolytes (SSEs), halide-based Na^+ SSEs offer high electrochemical stability but are limited by low ionic conductivity and poor thermal stability. Herein, a novel class of sodium hafnium chalcohalide SSEs is reported with a dual-anion (S^{2-}/Cl^-) framework, with a high ionic conductivity of 4.5×10^{-4} S cm^{-1}. The incorporation of sulfur enhances Na^+ mobility by reducing the migration barrier through increased anion polarizability and expanded diffusion pathways. Additionally, S^{2-} contributes to stronger interatomic bonding, leading to higher cohesive energy density, improved thermal stability, and mechanical robustness. These SSEs exhibit minimal sulfur oxidation and excellent chemical/electrochemical interface stability with different cathode materials, such as O3-layered $NaNi_{1/3}Fe_{1/3}Mn_{1/3}O_2$, P2/O3 layered $Na_{0.85}Mn_{0.5}Ni_{0.4}Fe_{0.1}O_2$, and $Na_3V_2(PO_4)_3$ cathodes. As a result, SSNIBs with P2/O3 layered $Na_{0.85}Mn_{0.5}Ni_{0.4}Fe_{0.1}O_2$ employing the sodium hafnium chalcohalide SSEs demonstrate outstanding cycling performance, achieving a capacity retention of 88.5% after 200 cycles at 0.1 C. This study establishes a new design strategy for high-performance SSEs, demonstrating that mixed-anion frameworks offer a viable route to overcome the intrinsic limitations of single-anion electrolytes in next-generation SSNIBs.

1. Introduction

Rechargeable Na-ion batteries (NIBs) have emerged as a promising alternative to lithium-ion batteries (LIBs) for large-scale energy storage systems and mid-range electric vehicles. Their growing interest is driven by the higher abundance and more even distribution of sodium in the Earth's crust compared to lithium.[1–3] Similar to commercial LIBs, current NIBs use organic liquid electrolytes, which provide high ionic conductivity and good wettability. However, their flammability and low thermal stability pose significant safety risks.[4,5] To mitigate these concerns, solid-state Na-ion batteries (SSNIBs) have been proposed as an optimal solution, offering key advantages such as enhanced safety, long-term stability, and the potential for high energy density.[6,7]

Na-based solid-state electrolytes (SSEs) serve as both ionic conductors and separators between the cathode and anode, making them essential components in SSNIBs. Ideal Na-ion SSEs should possess several key characteristics, including high

Z. L. Dong, Y. Gan, V. Martins, A. Mozafarighoraba, R. Zhang, C. Turner, H. Abdolvand, Y. Zhao
Department of Mechanical and Materials Engineering
University of Western Ontario
London, Ontario N6A 5B9, Canada
E-mail: yzhao628@uwo.ca

Y. Huang, T.-K. Sham
Department of Chemistry
University of Western Ontario
London, Ontario N6G 2V4, Canada
E-mail: tsham@uwo.ca

The ORCID identification number(s) for the author(s) of this article can be found under https://doi.org/10.1002/adfm.202516657

© 2025 The Author(s). Advanced Functional Materials published by Wiley-VCH GmbH. This is an open access article under the terms of the Creative Commons Attribution-NonCommercial License, which permits use, distribution and reproduction in any medium, provided the original work is properly cited and is not used for commercial purposes.

DOI: 10.1002/adfm.202516657

B. Sourav, P. Kaghazchi
Institute of Energy Materials and Devices
Materials Synthesis and Processing (IMD-2)
Forschungszentrum Jülich Gmb, H52425 Jülich, Germany
E-mail: p.kaghazchi@fz-juelich.de

X. Wang
X-ray Science Division
Argonne National Laboratory
Lemont, IL 60439, USA

X. Pang
CanmetMATERIALS
Natural Resources Canada 183 Longwood Road South, Hamilton, Ontario L8P0A5, Canada

P. Kaghazchi
MESA+ Institute for Nanotechnology
University of Twente
P. O. Box 217, Enschede 7500AE, The Netherlands

ionic conductivity to facilitate efficient ion transport, a wide electrochemical window to support high-voltage cathode materials, and excellent chemical and electrochemical stability to prevent rapid capacity degradation and short circuits. Additionally, they should exhibit strong mechanical properties to suppress dendrite growth and be easy to manufacture for practical application.[8,9] Among various types of Na SSEs, halide-based Na SSEs have received widespread attention due to their excellent electrochemical stability at high voltages and good cyclability when paired with suitable high-voltage oxide cathode materials.[10–12] Na_2ZrCl_6 and $NaAlCl_4$ were reported to have stable interfaces with the $NaCrO_2$ cathode.[13,14] However, the low ionic conductivity (1.8×10^{-5} S cm^{-1} for Na_2ZrCl_6 and 5.5×10^{-6} S cm^{-1} for $NaAlCl_4$) significantly limits the practical application of these SSEs in SSNIBs. Cation doping is a widely used strategy to improve ionic conductivity; for example, the ionic conductivity of Er- and Y-doped Na_2ZrCl_6 SSEs can reach 10^{-4} S cm^{-1}.[12,15] However, this approach is limited by the high cost of rare metals such as La, Y, In, and Sc, as well as performance constraints arising from a single-anion framework.[13,16]

More recently, a new family of halide SSEs featuring mixed-anion frameworks (particularly oxychloride-based systems for Li^+ and Na^+) has been discovered.[10,16,17] Compared with the single-anion framework, the mixed-anion framework can enhance both ionic conductivity and electrochemical performance by introducing the metal-chloride cluster and oxygen coner-sharing connectivity within metal-O-Cl polyhedral.[16,17] However, challenges remain, such as for Na oxychloride SSEs, which exhibit poor thermal stability at high temperatures (over 400 °C), leading to decomposition and oxygen release. To address these limitations, the exploration of alternative chalcogen-based anions (such as S and Se) for mixed anion frameworks is considered a promising approach.

In this study, we present a novel family of sodium hafnium chalcohalide SSEs characterized by dual-anion frameworks. Instead of using the traditional doping method, sulfur was chosen as the chalcogen anion to create a novel chalcohalide framework. Compared to the halide SSEs (sodium hafnium chlorine), the mixed anion chalcohalide framework (sodium hafnium sulfide chloride) exhibits a more compact morphology, improved thermal and mechanical properties. In addition, the mixed anion chalcohalide framework also demonstrates a more disordered Na^+ distribution, a reduced Na^+ migration barrier, and enhanced ionic conductivity due to the appearance of two different Na^+ environments within the SSE matrix. In contrast to the oxygen corner-sharing connectivity in oxychloride-based SSEs, sodium hafnium sulfide chloride SSEs exhibit a more complex local Hf coordination, featuring Hf–Cl/S edge-sharing, Cl corner-sharing units connected via Hf atoms, as well as isolated Hf–Cl/S units, with edge-sharing also occurring through mixed Cl–S edges. Furthermore, sodium hafnium sulfide chloride SSEs, which maintain minimal sulfur oxidation, demonstrate significantly improved chemical and electrochemical interface stability when paired with layered cathodes, in contrast to sodium hafnium chlorine SSEs. Consequently, SSNIBs with P2/O3 $Na_{0.85}Mn_{0.5}Ni_{0.4}Fe_{0.1}O_2$ layer cathodes using sodium hafnium sulfide chloride SSEs showcase exceptional stable performance, achieving a capacity retention of 88.5% after 200 cycles at 0.1 C. In addition, two commercial cathodes (O3-$NaNi_{1/3}Fe_{1/3}Mn_{1/3}O_2$, and $Na_3V_2(PO_4)_3$)-based SSNIBs utilizing sodium hafnium sulfide chloride SSEs also demonstrate significant stable performance, achieving a capacity retention of 88.8% after 150 cycles at 0.1 C, and 98.9% after 100 cycles at 0.1 C, respectively. This research extends the understanding of halide-based SSEs with dual-anion frameworks and paves the way for the design of high-performance SSNIBs by overcoming the limitations associated with single-anion frameworks through innovative structural designs, potentially transforming the technology of SSNIBs

2. Results and Discussion

The sodium hafnium chalcohalide SSEs were prepared by the ball-milling method using Na_2S and $HfCl_4$ as the precursors, with various stoichiometric ratios (Na_2S-x$HfCl_4$; x represents the molar ratio of $HfCl_4$: Na_2S; x ranges from 1.0 to 1.5). By the introduction of the S element, the sodium hafnium chalcohalide SSEs are formed from the sodium hafnium halide SSEs (**Figure 1a**). When the ratio of $HfCl_4$: Na_2S was 1.3 ($x = 1.3$), sodium hafnium chalcohalide SSEs demonstrated the highest ionic conductivity with 4.52×10^{-4} S cm^{-1} (Figure 1b; Figure S1a, Supporting Information). Electrochemical impedance spectroscopy (EIS) results for all sodium hafnium chalcohalide SSEs are depicted in Figures S1b,S2 (Supporting Information). The activation energies for sodium hafnium chalcohalide SSEs from Arrhenius plots were determined to be between 0.384 and 0.428 eV, indicating a low Na^+ migration barrier in sodium hafnium chalcohalide SSEs (Figure S1c, Supporting Information). To investigate the electronic conductivities of sodium hafnium chalcohalide SSEs, the DC polarization method was applied. As shown in Figure S3 (Supporting Information), the electronic conductivity of sodium hafnium chalcohalide SSEs was found to be $<10^{-10}$ S cm^{-1}, suggesting that the chalcohalide SSEs are good electronic insulators, hence beneficial for inhibiting electrical leakage and ensuring prolonged operational life in SSNIBs. Therefore, the Na_2S-1.3$HfCl_4$ (Na-Hf-S-Cl) SSEs show the highest ionic conductivity, low Na^+ migration barrier, and electronic conductivities, making them a representative example of sodium hafnium chalcohalide materials. To compare the difference between chalcohalide SSEs and chloride SSEs, Na-Hf-Cl SSEs were prepared with the same synthesis conditions, except Na_2S was replaced by NaCl. The EIS result suggests that the ionic conductivity of NaCl-1.3$HfCl_4$ (Na-Hf-Cl) SSEs is 7.5×10^{-5} S cm^{-1}, and the Arrhenius plots yield an activation energy of 0.387 eV for Na-Hf-Cl SSEs (Figure S4a–c, Supporting Information). Both results suggest that Na^+ diffusion in Na-Hf-Cl SSEs is much lower than in the Na-Hf-S-Cl SSEs. Although the DC polarization method suggests that the electronic conductivity of Na-Hf-Cl SSEs was $<10^{-10}$ S cm^{-1} as well (Figure S4d, Supporting Information), the low ionic conductivity may not satisfy the practical requirements of SSNIBs performance.

The thermal stability and physical properties of Na-Hf-S-Cl and Na-Hf-Cl SSEs were further investigated. The thermogravimetric analysis (TGA) was used to study the thermostability of Na-Hf-S-Cl and Na-Hf-Cl SSEs (Figure 1c). Notable differences in thermal stability were observed between the two compositions. The Na-Hf-S-Cl SSEs exhibit excellent thermal stability with minimum weight percentage loss (≈7.3%) until 600 °C. In contrast, the Na-Hf-Cl SSEs start to decompose ≈323 °C and display an

© 2025 The Author(s). Advanced Functional Materials published by Wiley-VCH GmbH

16163028, 2026, 8, Downloaded from https://advanced.onlinelibrary.wiley.com/doi/10.1002/adfm.202516657 by Forschungszentrum Jülich GmbH Research Center, Wiley Online Library on [28/01/2026]. See the Terms and Conditions (https://onlinelibrary.wiley.com/terms-and-conditions) on Wiley Online Library for rules of use; OA articles are governed by the applicable Creative Commons License

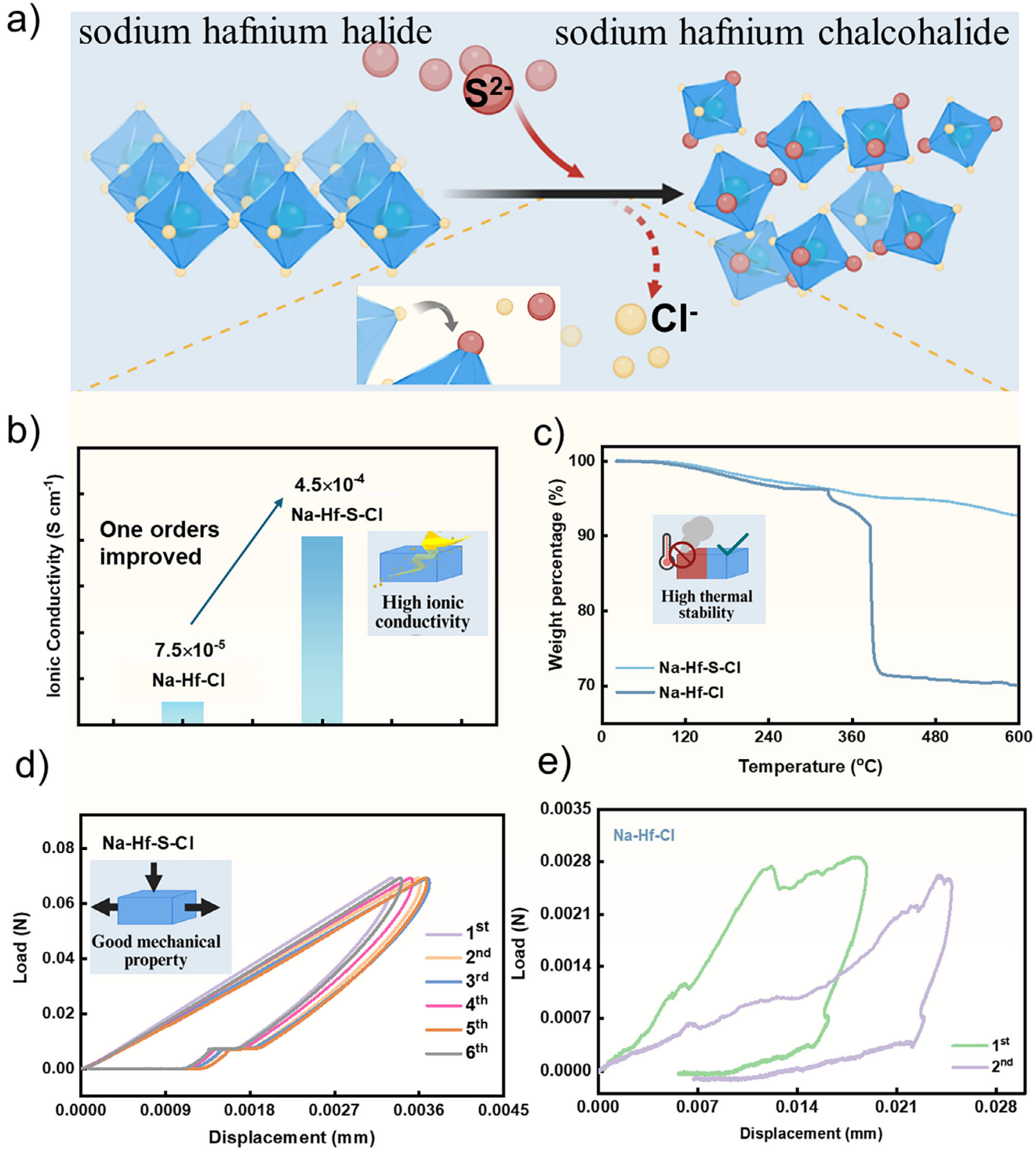

Figure 1. a) Schematics of the evolution from the sodium hafnium halide to sodium hafnium chalcohalide. The comparison between the Na-Hf-Cl and Na-Hf-S-Cl in terms of the b) ionic conductivity, c) TGA curve. The nanoindentation load-displacement curve of d) Na-Hf-S-Cl and e) Na-Hf-Cl.

undesirable 30% weight percentage loss due to the poor thermal stability of the Cl-rich structure. Compared with O^{2-} or S^{2-}, Cl^{-} forms weaker ionic bonds with metal; therefore, Cl-rich materials decompose more readily under heating.[16,18] The scanning electron microscope (SEM) images show that Na-Hf-S-Cl and Na-Hf-Cl SSEs have different pellet surfaces and cross-section morphologies (Figure S5, Supporting Information). Compared with Na-Hf-Cl SSEs, Na-Hf-S-Cl SSEs present more continuous and smoother surfaces and tighter cross sections. The mechanical properties of Na-Hf-S-Cl and Na-Hf-Cl SSEs were studied

© 2025 The Author(s). Advanced Functional Materials published by Wiley-VCH GmbH

16163028, 2026, 8, Downloaded from https://advanced.onlinelibrary.wiley.com/doi/10.1002/adfm.202516657 by Forschungszentrum Jülich GmbH Research Center, Wiley Online Library on [28/01/2026]. See the Terms and Conditions (https://onlinelibrary.wiley.com/terms-and-conditions) on Wiley Online Library for rules of use; OA articles are governed by the applicable Creative Commons License

using nanoindentation (Figure 1d,e). The modulus of Na-Hf-S-Cl SSEs was ≈2.86 GPa, and the load-displacement curve of Na-Hf-Cl SSEs demonstrates an almost negligible response to hardness or modulus. In addition, an obvious crack can be observed for Na-Hf-Cl SSEs during the indentation (Figure S6, Supporting Information). The differences in the mechanical properties between the two SSEs arise from their interatomic interactions. Metal—sulfur bonds are typically stronger and more covalent than metal—chlorine bonds, which tend to be more ionic and weaker. Furthermore, compared to Cl^-, the S^{2-} ion is more polarizable, facilitating stronger interatomic interactions. Consequently, the introduction of S^{2-} enhances the cohesive energy density and requires more energy to deform the unit structure, resulting in a higher hardness. The inferior mechanical properties observed in other chlorine-rich compositions further support this correlation.[19,20] In summary, Na-Hf-S-Cl chalcohalide SSEs exhibit higher ionic conductivity, more compact morphology, and better thermal and stiffer mechanical properties compared to Na-Hf-Cl halide SSEs.

To gain insights into the relationship between local structure and Na^+ diffusion of Na-Hf-S-Cl chalcohalide SSEs and Na-Hf-Cl halide SSEs, detailed structural analyses were performed. X-ray diffraction (XRD) was used to determine the crystallinity of Na_2S-x$HfCl_4$ and Na-Hf-Cl SSEs. The XRD pattern of Na-Hf-S-Cl and Na-Hf-Cl SSEs with references is exhibited in **Figure 2a**, and the XRD pattern for Na_2S-x$HfCl_4$ SSEs with different synthesis conditions is presented in Figure S7a (Supporting Information). As shown in Figure 2a, Na-Hf-S-Cl SSEs present an amorphous structure. In contrast, obvious XRD peaks can be found for Na-Hf-Cl SSEs, which demonstrate a similar crystal lattice of Na_2HfCl_6.[16] For Na_2S-x$HfCl_4$ SSEs with different precursor ratios, NaCl impurities can be found from the XRD patterns when ratios are low (Na_2S-1.0$HfCl_4$ and Na_2S-1.1$HfCl_4$). With increasing $HfCl_4$ content, the NaCl diffraction peaks gradually disappear, and a mixture of Na_2HfCl_6 crystalline phases and amorphous structures emerges. While NaCl is a common salt with intrinsically low ionic conductivity, and fully crystalline Na–Hf–Cl SSEs exhibit relatively poor conductivity (7.5×10^{-5} S cm^{-1}), the introduction of an amorphous phase significantly improves the overall ionic transport. This enhancement is attributed to the elimination of grain boundaries and the ease of forming thin films with uniform Na^+ pathways. Therefore, Na–Hf–S–Cl SSE composition with an optimal balance, which exhibits a predominantly amorphous structure with minimal Na_2HfCl_6 crystallites (Na_2S-1.3$HfCl_4$ SSEs) would provide the highest ionic conductivity due to the less grain boundary impedance and enhanced Na^+ diffusion.

Raman spectroscopy was used to further investigate the structure of Na-Hf-S-Cl chalcohalide SSEs and Na-Hf-Cl halide SSEs, respectively. Figure 2b exhibits the Raman spectra of Na-Hf-S-Cl SSEs and Na-Hf-Cl SSEs with $HfCl_4$ reference. A tiny peak can be found around 369 cm^{-1} in Na-Hf-Cl SSEs, which belongs to the A_1g mode of $Hf_2Cl_9^-$ group.[21] For Na-Hf-S-Cl SSEs, there is a significant peak located at around 334 cm^{-1}, which is attributed to the A_{1g} mode of HfS_2.[22,23] Na_2S-x$HfCl_4$ chalcohalide SSEs with different ratios also demonstrate the same HfS_2 structure stretching as Na-Hf-S-Cl SSEs, indicating the Hf-S and Hf-Cl local structures are the major structural components for the SSEs (Figure S7b, Supporting Information).

To study the local chemical information of Na-Hf-S-Cl chalcohalide SSEs, X-ray photoelectron spectroscopy (XPS) was conducted. Figure S8 (Supporting Information) exhibits the XPS spectra of S 2*p*, Cl 2*p*, Hf 4*f*, and Na 1*s* for Na-Hf-S-Cl SSEs, respectively. The C 1*s*was used as the energy calibration for all XPS measurements. The S 2*p* XPS spectra of Na-Hf-S-Cl SSEs exhibit four prominent peaks at a binding energy of 161.7, 162.8, 163.8, and 164.3 eV in S 2*p* XPS spectra of Na-Hf-S-Cl SSEs (Figure S8a, Supporting Information). The peaks at 161.7 eV (S $2p_{3/2}$) and 163.8 eV (S $2p_{1/2}$) belong to Na_2S,[24] while those at 162.8 eV (S $2p_{3/2}$) and 164.3 eV (S $2p_{1/2}$) are likely assigned to Hf-S interaction. Compared to HfS_2, the observed peaks exhibit a positive energy shift, suggesting that the S 2*p* hybridized photoelectrons in Na-Hf-S-Cl are influenced by the presence of Hf^{4+}. This implies that both Hf^{4+} and Na^+ are involved in the local chemical environment surrounding the S^{2-} anions within the SSEs matrix.[25,26] Furthermore, the Na 1*s* XPS spectra also suggest a ≈1 eV positive shift in binding energy relative to the Na 1*s* peaks in pristine Na_2S,[24] which is more likely due to a distorted environment, especially the interaction between Na^+ and chalcogen anions in a transition metal—chalcogenide bonding environment (i.e., Hf—S bonding).[27] This observation supports the hypothesis that S^{2-} anions act as one of the diffusion pathways for Na^+ ions, as further corroborated by the schematic in Figure S8b (Supporting Information). The Cl 2*p* XPS spectra (Figure S8c, Supporting Information) display characteristic peaks at 199.0 eV (Cl $2p_{3/2}$) and 200.6 eV (Cl $2p_{1/2}$), indicating that Cl^- is primarily coordinated with transition metal species (Hf), rather than with Na^+.[28,29] Additionally, with Hf 4*f* XPS spectrum (Figure S8d, Supporting Information) reveals contributions from both HfS_2 and $HfCl_4$, which is in agreement with the S 2*p* and Cl 2*p* XPS findings.[25,26,30]

To investigate the local chemical structure of Na-Hf-S-Cl SSEs, pair distribution function (PDF) and Extended X-ray absorption fine structure (EXAFS) were carried out (Figure 2c,d; Figure S9, Supporting Information). Figure 2c demonstrates the PDF results of Na-Hf-S-Cl SSEs. Since the Hf—S and Hf—Cl bonds have a similar bonding distance, both Hf—S and Hf—Cl bonds may be present in Na-Hf-S-Cl SSEs at ≈2.5 Å.[16,31] Furthermore, the crystallographic information framework of HfS_2 (mp-985829) reveals that the peak observed at approximately 3.5 Å is attributed to the Hf-Hf bonding within the HfS_2 crystal. This primarily indicates the sulfur concentration within the Hf-centered polyhedron. To quantitatively understand the coordination environment around the central Hf in Na-Hf-S-Cl SSEs, Hf L_3-edge EXAFS spectroscopy was utilized as shown in Figure 2d (FT of the EXAFS) and Figure S9b (Supporting Information) (EXAFS in k space). The EXAFS fitting provides the average coordination information nearest to Hf in Na-Hf-S-Cl, as shown in Table S1 (Supporting Information). As illustrated in Figure 2d, there is one Hf-S path located at 3.22 Å, and two Hf-Cl coordinated environments located at 2.45 and 2.98 Å, respectively. According to the fitting results, a central Hf atom is surrounded by ≈2.42 sulfur, 2.77 $chlorine_1$, and 3.19 $chlorine_2$ atoms (Table S1, Supporting Information).

To elucidate the local chemical and electronic environment of sodium ions, high-resolution solid-state ^{23}Na magic angle spinning (MAS) nuclear magnetic resonance (NMR) spectroscopy was employed. Figure 2e presents the room temperature ^{23}Na

© 2025 The Author(s). Advanced Functional Materials published by Wiley-VCH GmbH

16163028, 2026, 8, Downloaded from https://advanced.onlinelibrary.wiley.com/doi/10.1002/adfm.202516657 by Forschungszentrum Jülich GmbH Research Center, Wiley Online Library on [28/01/2026]. See the Terms and Conditions (https://onlinelibrary.wiley.com/terms-and-conditions) on Wiley Online Library for rules of use; OA articles are governed by the applicable Creative Commons License

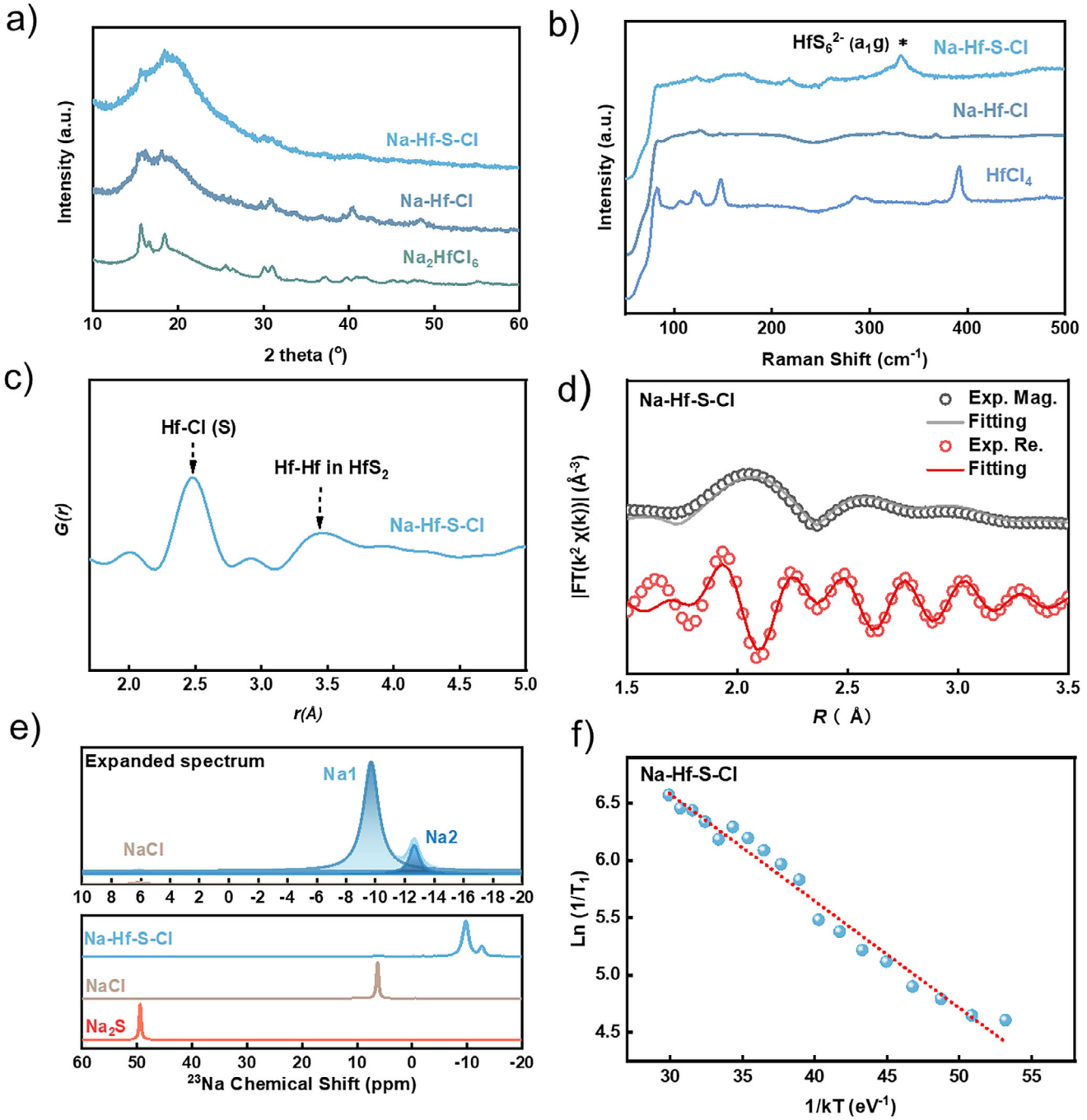

Figure 2. a) The XRD pattern of Na-Hf-S-Cl, Na-Hf-Cl, and Na_2HfCl_6 SSEs; b) the Raman spectra of Na-Hf-S-Cl, Na-Hf-Cl SSEs, and $HfCl_4$; c) the PDF spectra of Na-Hf-S-Cl SSEs; d) the Fourier Transform of the Hf L_3-edge EXAFS of Na-Hf-S-Cl SSEs in R space; e) ^{23}Na MAS spectra acquired at 14.3 T under a spinning rate of 20 kHz; i) Temperature-dependent ^{23}Na spin-lattice relaxation rates measured in the laboratory frame for Na-Hf-S-Cl SSEs.

MAS NMR spectrum of the Na-Hf-S-Cl SSE alongside those of reference materials Na_2S and NaCl. The spectrum reveals three distinct resonances at 6.1, −9.7, and −12.7 ppm. The resonance at 6.1 ppm corresponds to NaCl, indicating a minor impurity phase, while the signals at −9.7 ppm (Na1) and −12.7 ppm (Na_2) are assigned to Na^+ ions within the SSE matrix. These chemical shifts are characteristic of Na^+ sites coordinated with six chloride ions in a prismatic geometry, consistent with previous reports.[15,32] The chemical shift difference between Na1 and Na2 is attributed to variations in the second coordination sphere, specifically the presence of Hf $^{4+}$ ions. It has been established that increased Hf $^{4+}$ coordination in the second shell results in a more negative chemical shift for ^{23}Na.[15] Quantitative spectral fitting indicates that NaCl constitutes ≈1% of the total sodium species, whereas the Na1and Na2 sites account for 85% and 14%, respectively. The absence of a resonance near 49 ppm, characteristic of Na_2S,

© 2025 The Author(s). Advanced Functional Materials published by Wiley-VCH GmbH

16163028, 2026, 8, Downloaded from https://advanced.onlinelibrary.wiley.com/doi/10.1002/adfm.202516657 by Forschungszentrum Jülich GmbH Research Center, Wiley Online Library on [28/01/2026]. See the Terms and Conditions (https://onlinelibrary.wiley.com/terms-and-conditions) on Wiley Online Library for rules of use; OA articles are governed by the applicable Creative Commons License

suggests complete consumption of the Na_2S precursor and that sulfur atoms are predominantly coordinated to Hf^{4+}, rather than Na^+. The Gaussian line shapes observed for Na1 and Na2 sites have a full width at half maximum (FWHM) of 196 and 130 Hz, respectively, which is significantly larger than the FWHM of crystalline NaCl (67 Hz). This implies a significant structural disorder around the local environment of Na^+ ions.

To investigate sodium dynamics, variable-temperature ^{23}Na static NMR measurements were conducted at a lower magnetic field. Due to the lower resolution at reduced magnetic field strength, only one broad signal was observed, as opposed to the two distinct resonances observed in high-resolution spectra acquired at higher magnetic fields. At lower temperatures, a single broad resonance with an FWHM of ca. 925 Hz is observed, representing the convolution of Na1 and Na2 environments (Figure S10, Supporting Information). The linewidth narrows to ≈550 Hz near room temperature and then broadens again upon heating. At room temperature, convergence of the chemical shifts for both sites is observed, supporting the notion of rapid Na^+ hopping between the two sites.[33] Spin-lattice relaxation rate (1/T1) measurements were carried out to quantify sodium ion mobility. A plot of $\ln(1/T_1)$ versus reciprocal temperature (1/kT) is shown in Figure 2f, from which an activation energy of 0.09 eV was extracted. This activation energy reflects the intrinsic Na^+ mobility within the bulk lattice and is typically lower than values obtained from EIS, which measures macroscopic ionic transport including grain boundaries and interfacial resistances.[34]

In summary, we tentatively assign Na1 (85%) to Na^+ primarily coordinated to sulfide-rich regions of the network – these Na ions stabilize the glass structure by balancing the charge of Hf—S bonds or possibly terminal S^{2-} anions. They exhibit a broader NMR lineshape and likely serve as the more static Na inventory of the solid electrolyte. Na2 (14%), on the other hand, might correspond to Na^+ in chloride-rich coordination environments – possibly in or near the $HfCl_6$-like polyhedral units or at interfaces between $HfCl_6$and HfSCl units. These Na2 ions are likely the dynamic species that facilitate ion conduction: they occupy transitional sites along the diffusion pathways (hopping between adjacent Hf-centered polyhedra through shared Cl bridges). Even though they are fewer in number, they are likely to show higher mobility and carry a disproportionate amount of the Na-ion current. It has been previously shown that a Cl-rich sulfide-chloride glass had higher ionic conductivity specifically due to its "unique chloride-bridging structure," which provides low-barrier Na migration pathways.[35] In summary, Na1 can be viewed as the reservoir of Na^+ (anchored to the lattice framework), while Na2 is the diffusional "vehicles" that hop between those reservoirs. This model aligns with the concept of "defect-mediated" conduction seen in other dual-anion conductors: only a small fraction of Na^+ needs to be in the right coordination environment (or activated state) at any time to achieve high overall conductivity.

The atomistic structure of Na-Hf-S-Cl SSEs was calculated using density functional theory (DFT) to enable a direct comparison with experimental pair distribution function (PDF) data. The DFT-optimized structural model, shown in **Figure 3**, reveals that Hf ions are coordinated by both sulfur and chlorine atoms, forming a range of local environments. Specifically, from our calculations, three distinct types of Hf_2centered polyhedra were identified: i) edge-sharing Hf–Cl/S units, ii) corner-sharing Hf units linked via Cl atoms, and iii) isolated Hf–Cl/S units. Notably, edge-sharing interactions also occur through mixed Cl–S edges, suggesting a degree of structural complexity in the local Hf coordination. Theoretical PDF calculated from the fully relaxed structure shows an average Hf–Hf distance of 3.47 Å, in good agreement with the experimental PDF peak observed at ~3.5 Å, which is attributed to Hf–Hf interactions within Hf-centered polyhedra in Na-Hf-S-Cl SSEs, as corroborated by comparison with the HfS_2 crystallographic reference (Figure 2c). Furthermore, the calculated average bond lengths of Hf—S and Hf—Cl are ≈2.3 Å, which closely match the experimental PDF signal ≈2.5 Å. This is consistent with the interpretation that both Hf—S and Hf—Cl bonds contribute to the local structure (Figure 2c). The good agreement between the DFT-predicted local structure and the experimental PDF and EXAFS measurements validates the theoretical model and underscores the presence of mixed-anion coordination environments around Hf in this complex halide-sulfide SSE system.

In summary, the incorporation of S^{2-} anions into the Na-Hf-Cl system induces pronounced local structural rearrangements, leading to the formation of amorphous Na-Hf-S-Cl SSEs. This amorphization, absent in the crystalline halide analogues lacking sulfur, effectively eliminates resistive grain boundaries and thereby facilitates enhanced Na^+ ion transport.[16] In the resulting dual-anion chalcohalide framework, sulfur atoms preferentially coordinate with high-valent Hf^{4+} centers rather than with Na^+ ions, generating a more open and disordered network structure. This configuration not only promotes facile Na^+ migration[36] but also contributes to the significantly improved ionic conductivity and reduced activation energy observed in Na-Hf-S-Cl SSEs compared to their Na-Hf-Cl counterparts. Moreover, detailed structural analysis reveals the coexistence of three distinct types of Hf-centered polyhedral motifs: i) edge-sharing Hf–Cl/S polyhedra, ii) corner-sharing polyhedra connected via bridging Cl atoms, and iii) isolated Hf–Cl/S units. Notably, the edge-sharing linkages involve mixed Cl—S coordination, underscoring the increased local structural complexity introduced by the mixed-anion environment. These unique structural features, arising from the integration of chalcogenide and halide chemistries, collectively underpin the superior Na^+ conduction properties of Na-Hf-S-Cl chalcohalide SSEs.

To compare the influence of two SSEs on electrochemical performance, linear sweep voltammetry (LSV), cyclic voltammetry (CV), and SSNIB evaluations were conducted (Figure S11, Supporting Information). As depicted in Figure S12a (Supporting Information), the potential of Na-Hf-S-Cl SSEs was scanned from the open-circuit voltage (OCV) to 6 V, revealing decomposition starting at ≈3.7 V, while Na-Hf-Cl SSEs began to decompose ≈4.1 V. Both SSEs exhibited a higher oxidation potential than traditional sulfide-based Na SSEs, such as NAS and NPS, which typically decompose ≈2.5V.[37,38] Notably, Na-Hf-S-Cl SSEs demonstrated a smaller oxidation potential than Na-Hf-Cl SSEs due to the presence of S^{2-}, indicating that the Cl^- anion may inhibit the oxidation of Hf—S bonds at elevated potentials. This significantly enhances electrochemical stability and may entail compatibility with high-voltage cathodes. When the potential decreased from OCV to 1 V, both Na-Hf-S-Cl and Na-Hf-Cl SSEs exhibited decomposition at ≈2.5 V, and the decomposition of Na-Hf-Cl SSEs was more pronounced than that of Na-Hf-S-Cl SSEs,

© 2025 The Author(s). Advanced Functional Materials published by Wiley-VCH GmbH

16163028, 2026, 8, Downloaded from https://advanced.onlinelibrary.wiley.com/doi/10.1002/adfm.202516657 by Forschungszentrum Jülich GmbH Research Center, Wiley Online Library on [28/01/2026]. See the Terms and Conditions (https://onlinelibrary.wiley.com/terms-and-conditions) on Wiley Online Library for rules of use; OA articles are governed by the applicable Creative Commons License

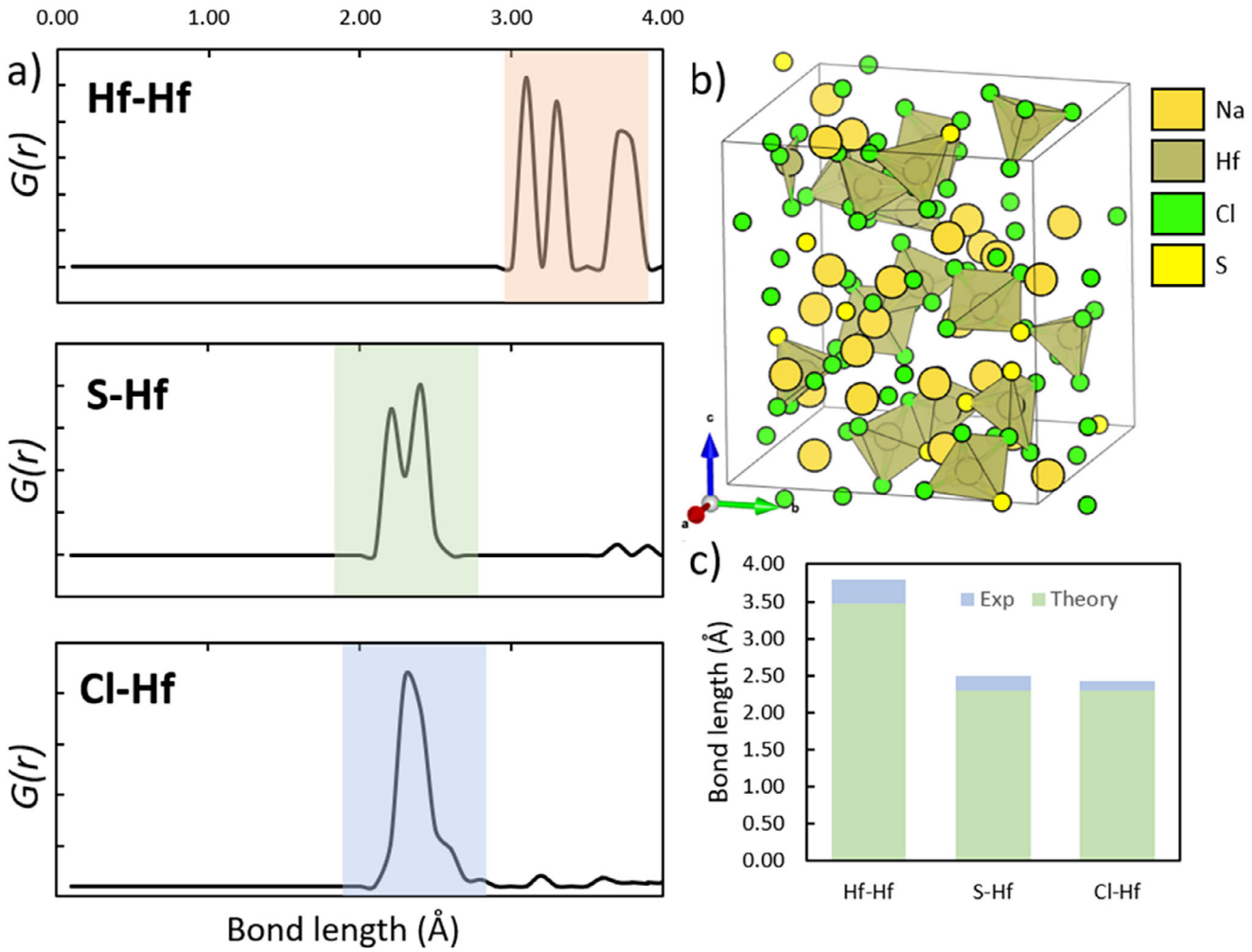

Figure 3. a) Theoretical pair distribution function (PDF) of Na-Hf-S-Cl from b) the DFT-optimized atomistic structure of amorphous Na-Hf-S-Cl, illustrating the local coordination environments. c) Comparison of average bond lengths derived from experimental and theoretical analyses, highlighting the agreement between DFT predictions and PDF/EXAFS measurements.

suggesting that both SSEs have relatively poor stability at the anode, with Na-Hf-Cl SSEs being worse. The inferior anode stability is a common issue for most sulfide and halide-based Na SSEs.[16,39,40] Figure S12b,c (Supporting Information) presents the CV profile of the SSNIBs using Na-Hf-S-Cl and Na-Hf-Cl SSEs at a scan rate of 0.2 mV S^{-1} for 5 cycles, respectively. The CV profiles of Na-Hf-S-Cl SSNIBs exhibited redox reaction peaks similar to those reported in previous studies.[16] In contrast, the CV profiles of Na-Hf-Cl SSNIBs showed an almost negligible response current compared to the Na-Hf-S-Cl SSNIBs, attributed to the low ionic conductivity of SSEs (0.75×10^{-4} S cm^{-1}), which hindered Na^+ ion diffusion during electrochemical cycling at room temperature. Nevertheless, both SSNIBs demonstrated good electrochemical reversibility, with overlapping oxidation and reduction peaks in CV.

The electrochemical performances of the SSNIBs using two SSEs are illustrated in **Figure 4**. Figure 4a displays the charge-discharge profiles for the Na-Hf-S-Cl SSNIBs based on $Na_{0.85}Mn_{0.5}Ni_{0.4}Fe_{0.1}O_2$ cathode at a rate of 0.1 C (1 C = 120 mAh g^{-1}). The initial three cycles were conducted at 0.05 C for activation, followed by measurements at 0.1 C. The initial reversible discharging capacity at 0.1 C is 115.4 mAh g^{-1}, with a Coulombic efficiency of 97.2%, indicating excellent compatibility and stability between the Na-Hf-S-Cl SSEs and $Na_{0.85}Mn_{0.5}Ni_{0.4}Fe_{0.1}O_2$ cathode. In contrast, the Na-Hf-Cl SSNIBs with the same cathode exhibit a significantly lower discharging capacity of 43.1 mAh g^{-1}, attributed to the low ionic conductivity of the SSEs (Figure 4b). Figure 4c,d displays the rate performances of both Na-Hf-S-Cl and Na-Hf-Cl SSNIBs based on the $Na_{0.85}Mn_{0.5}Ni_{0.4}Fe_{0.1}O_2$ cathode. As shown in Figure 4c and Figure S12d (Supporting Information), the reversible discharge capacities of 125.2, 113.4, 101.5,76.2, 61.1, and 18.3 mAh g^{-1} were achieved at 0.1 C, 0.2 C, 0.3 C, 0.4 C, 0.5 C, and 1.0 C, respectively, by Na-Hf-S-Cl SSNIBs. The low ionic conductivity of the NPS interlayer significantly constrained the achievable capacities at higher rates. Nevertheless, the cell retained 95.7% (119.8 mAh g^{-1}) of its initial capacity when the C-rate was reverted to 0.1 C further confirming the excellent electrochemical stability and compatibility between chalcohalide SSEs and layered cathode. In contrast, the reversible discharge capacities of 52.9, 27.7, and 8 mAh g^{-1} were

© 2025 The Author(s). Advanced Functional Materials published by Wiley-VCH GmbH

16163028, 2026, 8, Downloaded from https://advanced.onlinelibrary.wiley.com/doi/10.1002/adfm.202516657 by Forschungszentrum Jülich GmbH Research Center, Wiley Online Library on [28/01/2026]. See the Terms and Conditions (https://onlinelibrary.wiley.com/terms-and-conditions) on Wiley Online Library for rules of use; OA articles are governed by the applicable Creative Commons License

16163028, 2026, 8, Downloaded from https://advanced.onlinelibrary.wiley.com/doi/10.1002/adfm.202516657 by Forschungszentrum Jülich GmbH Research Center, Wiley Online Library on [28/01/2026]. See the Terms and Conditions (https://onlinelibrary.wiley.com/terms-and-conditions) on Wiley Online Library for rules of use; OA articles are governed by the applicable Creative Commons License

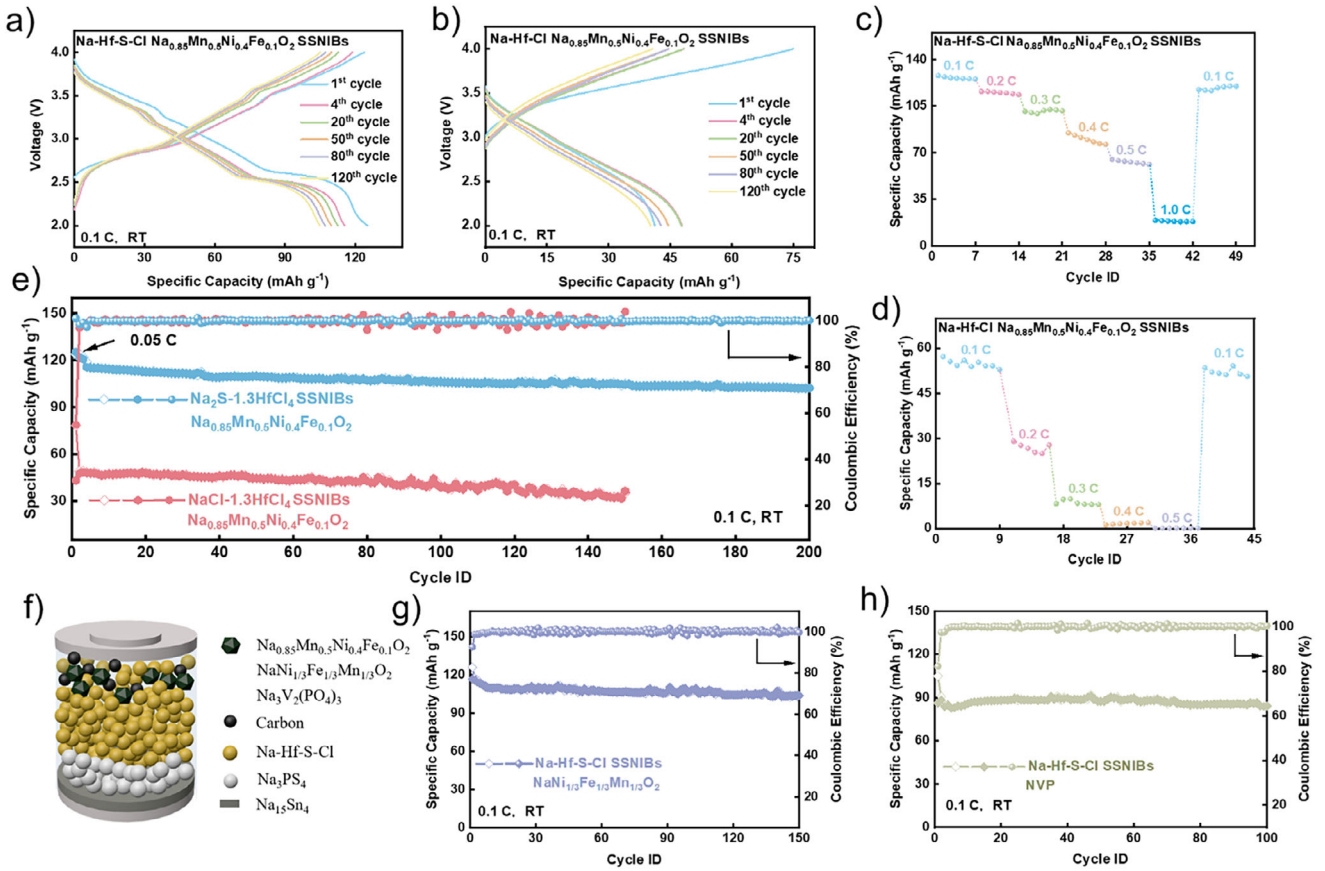

Figure 4. The charge-discharge profile of SSNIBs employing a) Na-Hf-S-Cl SSEs and b) Na-Hf-Cl SSEs with $Na_{0.85}Mn_{0.5}Ni_{0.4}Fe_{0.1}O_2$ cathode. The rate performance of SSNIBs employing c) Na–Hf–S–Cl SSEs and d) Na–Hf–Cl SSEs with $Na_{0.85}Mn_{0.5}Ni_{0.4}Fe_{0.1}O_2$ cathode. e) The cycling performance of Na-Hf-S-Cl and Na-Hf-Cl SSNIBs at 0.1 C under room temperature with $Na_{0.85}Mn_{0.5}Ni_{0.4}Fe_{0.1}O_2$ cathode. f) The schematic diagram of the cell structure with various cathodes. The cycling performance of Na-Hf-S-Cl SSNIBs with g) $NaNi_{1/3}Fe_{1/3}Mn_{1/3}O_2$ and h) NVP cathodes.

achieved at 0.1 C, 0.2 C, and 0.3 C, respectively, for the Na-Hf-Cl SSNIBs (Figure 4d; Figure S13a, Supporting Information). At current densities of 0.4 C and 0.5 C, the discharge capacities were nearly undetectable. Although the cell maintained 97.11% (51.3 mAh g^{-1}) of its original capacity when the C-rate was reverted to 0.1 C, the low specific capacity limits the practical compatibility of Na-Hf-Cl SSEs.

The cycling performance of Na-Hf-S-Cl SSNIBs with $Na_{0.85}Mn_{0.5}Ni_{0.4}Fe_{0.1}O_2$ cathode also demonstrates remarkable electrochemical stability at 0.1 C, as depicted in Figure 4e. These SSNIBs maintain a high reversible capacity of 102.2 mAh g^{-1} after 200 cycles, achieving a Coulombic efficiency of 100.2%, and a capacity retention of ≈88.5%. In comparison, the Na-Hf-Cl SSNIBs can only sustain a reversible capacity of 31.6 mAh g^{-1} after 150 cycles at 0.1 C. The differences between Na-Hf-S-Cl and Na-Hf-Cl SSNIB further suggest that the mixed Cl—S coordination in chalcohalide frameworks can enhance the ionic conductivity of SSEs and the electrochemical interface stability with the layered oxide cathodes compared to single-anion framework halide-based SSEs. Additionally, Figure S13b (Supporting Information) presents charge-discharge profiles for Na-Hf-S-Cl SSNIBs with $Na_{0.85}Mn_{0.5}Ni_{0.4}Fe_{0.1}O_2$ cathode at 0.3 C. The initial three cycles were conducted at 0.1 C for activation, followed by measurements at 0.3 C. The initial reversible discharging capacity measured at 0.3 C was 101.6 mAh g^{-1}. The cycling performances of the Na-Hf-S-Cl SSNIBs were evaluated at a higher current density of 0.3 C in Figure S13c (Supporting Information). The Na-Hf-S-Cl SSNIBs exhibit stable cycling performance and gradual capacity fading, achieving a specific capacity of 71.8 mAh g^{-1} after 450 cycles, with a Coulombic efficiency of 103.5%.

To examine the compatibility between Na-Hf-S-Cl chalcohalide SSEs and other commercial cathode materials, O3-layered cathode ($NaNi_{1/3}Fe_{1/3}Mn_{1/3}O_2$), and $Na_3V_2(PO_4)_3$ (NVP) cathode-based SSNIBs are also investigated (Figure 4f). Figure S14a (Supporting Information) displays the charge–discharge profiles for the Na-Hf-S-Cl-$NaNi_{1/3}Fe_{1/3}Mn_{1/3}O_2$ SSNIBs at a rate of 0.1 C (1 C = 120 mAh g^{-1}). The initial reversible discharging capacity at 0.1 C is 116.7 mAh g^{-1}, suggesting excellent compatibility and stability between the Na-Hf-S-Cl SSEs and O3 layered cathode. In addition, the Na-Hf-S-Cl-$NaNi_{1/3}Fe_{1/3}Mn_{1/3}O_2$ SSNIBs demonstrate outstanding electrochemical cycling stability at 0.1 C, as presented in Figure 4g. These SSNIBs maintain a high reversible capacity of 103.6 mAh g^{-1} after 150 cycles, achieving a Coulombic efficiency of 99.7%, and a capacity retention of 88.8%. Figure S14b (Supporting Information) and c displays the

© 2025 The Author(s). Advanced Functional Materials published by Wiley-VCH GmbH

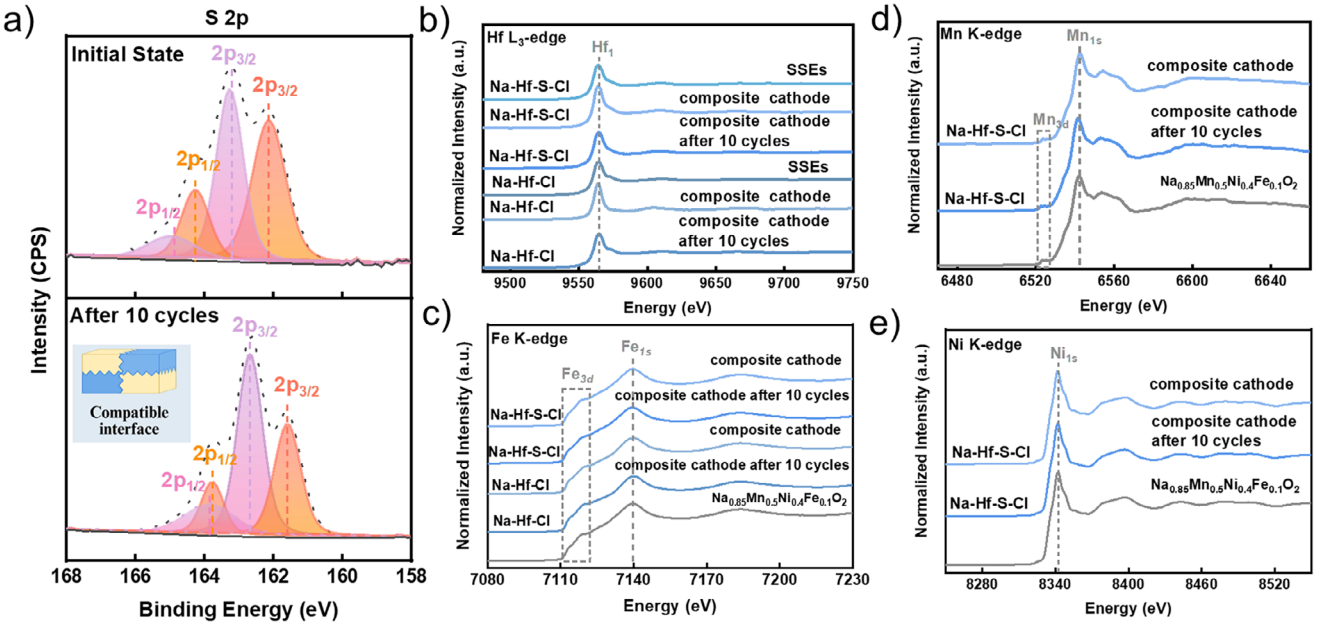

Figure 5. a) The S 2p XPS spectrum of Na-Hf-S-Cl composite cathode before cycling and after the 10th cycle; b) the Hf L_3-edge XANES spectrum of Na-Hf-S-Cl and Na-Hf-Cl SSEs and their cathode composite before cycling and after 10 cycles; c) the Fe K-edge XANES spectrum of Na-Hf-S-Cl SSEs and its cathode composite before cycling and after 10 cycles; d) the Mn K-edge XANES spectrum of Na-Hf-S-Cl SSEs and its cathode composite before cycling and after 10 cycles; e) the Ni K-edge XANES spectrum of Na-Hf-S-Cl SSEs and its cathode composite before cycling and after 10 cycles.

rate performances of Na-Hf-S-Cl-$NaNi_{1/3}Fe_{1/3}Mn_{1/3}O_2$ SSNIBs. The reversible discharge capacities of 128.7, 103.8, 75.7, 36.9, and 12.8 mAh g^{-1} were achieved at 0.1 C, 0.2 C, 0.3 C, 0.4 C, and 0.5 C, respectively by Na-Hf-S-Cl-$NaNi_{1/3}Fe_{1/3}Mn_{1/3}O_2$ SSNIBs. The low achievable capacities at higher rates are due to the low ionic conductivity of the NPS interlayer and partially irreversible Fe^{3+}/Fe^{4+} redox during the electrochemical reactions.[41] Even though the cell retained 99.7% (128.36 mAh g^{-1}) of its initial capacity when the C rate was reverted to 0.1 C, which more verifies the strong interfacial compatibility and stability between the chalcohalide anion frameworks and Na oxide layered cathodes. In addition, the Na-Hf-S-Cl-NVP SSNIBs demonstrate extremely stable cycling performance, achieving a specific capacity of 84.3 mAh g^{-1} after 100 cycles, with a Coulombic efficiency of 100.4%, and a capacity retention of 98.9% (Figure 4h). The SSNIB performances strongly demonstrate that the Na-Hf-S-Cl chalcohalide SSEs have excellent electrochemical stability and compatibility with various Na cathode materials.

To understand the electrochemical behaviour of Na-Hf-S-Cl SSNIBs, the interfacial chemistry of SSEs in the $Na_{0.85}Mn_{0.5}Ni_{0.4}Fe_{0.1}O_2$ cathode composite was studied using X-ray absorption near edge structure (XANES) and XPS (Figure 5 and Figure S15, Supporting Information). The S 2*p* XPS spectrum of the Na-Hf-S-Cl composite cathode was examined both before cycling and after the 10th cycle presented (**Figure 5a**). There is no significant peak shifting, indicating the stable local electrochemical environment for sulfur in the Na-Hf-S-Cl composite cathode following oxidation/reduction reactions. To further investigate the central Hf in Na-Hf-S-Cl SSEs after interaction with the $Na_{0.85}Mn_{0.5}Ni_{0.4}Fe_{0.1}O_2$ cathode during cycling, we measured both Hf L_3-edge XANES spectra and Hf 4*f* XPS spectra of the Na-Hf-S-Cl composite cathode before cycling and after the 10th cycle, respectively (Figure 5b; Figure S15a, Supporting Information). As shown in Figure 5b, there are no noticeable changes in the white line feature among Na-Hf-S-Cl SSEs and their composite cathode before cycling and after the 10th cycle, demonstrating that the local chemical environment of Hf in the Na-Hf-S-Cl unit cell remains unchanged during electrochemical performance. The Hf 4*f* XPS spectra corroborate the results from the Hf L_3-edge XANES spectra (Figure S15a, Supporting Information). Both X-ray characteristics and results indicate that the structure of the Hf polyhedron in the Na-Hf-S-Cl unit cell maintains its chemical and electrochemical stability during chemical and electrochemical reactions. Additionally, the Cl 2*p* XPS spectra and Na 1*s* spectra results show no significant peak shifting, suggesting that the stable local electrochemical environment of chlorine and sodium is preserved within the Na-Hf-S-Cl composite cathode throughout the redox processes (Figure S15b,c, Supporting Information).

To further understand the local chemical environment of transition metals in the $Na_{0.85}Mn_{0.5}Ni_{0.4}Fe_{0.1}O_2$ cathode affected by the SSEs, we measured the Fe K-edge, Mn K-edge, and Ni K-edges of the Na-Hf-S-Cl composite cathode before the cycling and after the 10th cycle (Figure 5c–e). The K-edge XANES spectra of the interested elements (Fe, Mn, and Ni) in the $Na_{0.85}Mn_{0.5}Ni_{0.4}Fe_{0.1}O_2$ cathode were also tested as the reference. Comparing the white-line features of the Fe K-edge, Mn K-edge, and Ni K-edges for the $Na_{0.85}Mn_{0.5}Ni_{0.4}Fe_{0.1}O_2$ cathode and the Na-Hf-S-Cl composite cathode before cycling and after the 10th cycle, no evident changes were observed, indicating that the local chemical environments of these elements in the layered cathode remain stable. The notable chemical and electrochemical stability between Na-Hf-S-Cl chalcohalide SSEs and layered $Na_{0.85}Mn_{0.5}Ni_{0.4}Fe_{0.1}O_2$

© 2025 The Author(s). Advanced Functional Materials published by Wiley-VCH GmbH

16163028, 2026, 8, Downloaded from https://advanced.onlinelibrary.wiley.com/doi/10.1002/adfm.202516657 by Forschungszentrum Jülich GmbH Research Center, Wiley Online Library on [28/01/2026]. See the Terms and Conditions (https://onlinelibrary.wiley.com/terms-and-conditions) on Wiley Online Library for rules of use; OA articles are governed by the applicable Creative Commons License

cathode accounts for the excellent cycling performance observed in Na-Hf-S-Cl SSNIBs.

Furthermore, we measured the Hf L_3-edge and Fe K-edge XANES spectra of Na-Hf-Cl composite cathode before cycling and after the 10th cycle to investigate the local chemical environment of Hf and Fe in Na-Hf-Cl SSNIBs, respectively (Figure 5b,c). As shown in Figure 5b, there are minor post-edge changes in the Na-Hf-Cl composite cathode after mixing, suggesting some hybridization has occurred. The general white-line feature among Na-Hf-Cl SSEs and its composite cathode before cycling and after the 10th cycle remains consistent, indicating that the local chemical environment of Hf in Na-Hf-Cl SSNIBs does not change during cycling performance. In the Fe K-edge XANES spectra, the general features of the Na-Hf-Cl composite cathode before cycling and after the 10th cycle are identical, implying the local chemical environment of Fe in Na-Hf-Cl SSNIBs remains stable during electrochemical reactions (Figure 5c). The low ionic conductivity of Na-Hf-Cl SSEs leads to reduced battery performance compared to Na-Hf-S-Cl SSNIBs. Collectively, the complex hafnium chalcohalide coordination enhances the ionic conductivity of the Na-Hf-S-Cl SSEs in the composite cathode, preserves the chalcohalide frameworks in SSEs, and stabilizes the local chemical environment of the $Na_{0.85}Mn_{0.5}Ni_{0.4}Fe_{0.1}O_2$ cathode, thereby contributing to the high capacity and excellent stability of the SSNIBs

3. Conclusion

In summary, this work presents innovative mixed-anion frameworks of Na-Hf-S-Cl chalcohalide SSEs. The unique corner-sharing Hf—Cl and edge-sharing mixed Hf—Cl/S and isolated Cl-S coordinated units demonstrate exceptional ionic conductivity, exceeding 10^{-4} S cm^{-1}, which surpasses that of Na-Hf-Cl halide SSEs. Compared to Cl^- ions, S^{2-} ions possess greater size and polarizability due to their softer characteristics, significantly lowering the barrier to ion migration. The enlarged diffusion channels further enhance the transport of Na^+, resulting in improved ionic conductivity. Additionally, S^{2-} ions strengthen interatomic interactions, leading to increased cohesive energy density and enhanced resistance to structural deformation, thereby improving both mechanical hardness and thermal stability. Importantly, the Na-Hf-S-Cl chalcohalide SSEs exhibit electrochemical stability and compatibility with various cathode materials, including O3-layered, P2/O3-layered, and NVP cathodes. The solid-state Na-ion batteries utilizing sulfur-chlorine mixed-anion SSEs show significantly enhanced electrochemical performance compared to single-halide systems. Overall, this work not only advances halide-based Na-ion SSEs but also introduces a promising design strategy for mixed-anion electrolytes, paving the way for future innovations in solid-state battery technologies.

Supporting Information

Supporting Information is available from the Wiley Online Library or from the author.

Acknowledgements

Z.L.D., B.S., and Y.G. contributed equally to this work. Y.Z. gratefully acknowledges financial support from the Natural Sciences and Engineering Research Council of Canada (NSERC), the Canada Foundation for Innovation (CFI), Mitacs, and the University of Western Ontario. T.K. Sham acknowledges financial support from NSERC and the Canada Research Chairs (CRC) program. Synchrotron measurements were conducted at the 12-BM-B beamline (Multipurpose X-ray Absorption and Scattering) of the Advanced Photon Source (APS), a U.S. Department of Energy (DOE) Office of Science User Facility operated by Argonne National Laboratory under Contract No. DE-AC02-06CH11357. Additional experiments were carried out at the HXMA and BXDS-WHE beamlines of the Canadian Light Source (CLS). The CLS is supported by CFI, NSERC, the National Research Council (NRC), the Canadian Institutes of Health Research (CIHR), the Government of Saskatchewan, and the University of Saskatchewan. The authors sincerely thank Dr. Ning Chen (HXMA beamline) and Dr. Graham King (BXDS-WHE beamline) at the CLS for their valuable technical support.

Conflict of Interest

The authors declare no conflict of interest.

Data Availability Statement

The data that support the findings of this study are available from the corresponding author upon reasonable request.

Keywords

DFT calculation, dual-anion framework, sodium chalcohalide solid electrolytes, solid-state sodium batteries, synchrotron X-ray techniques

Received: June 30, 2025
Revised: July 25, 2025
Published online: August 16, 2025

[1] A. Rudola, R. Sayers, C. J. Wright, J. Barker, *Nat. Energy* **2023**, *8*, 215.
[2] Y. Wu, W. Shuang, Y. Wang, F. Chen, S. Tang, X.-L. Wu, Z. Bai, L. Yang, J. Zhang, *Electrochem. Energy Rev.* **2024**, *7*, 17.
[3] W. Zuo, A. Innocenti, M. Zarrabeitia, D. Bresser, Y. Yang, S. Passerini, *Acc. Chem. Res.* **2023**, *56*, 284.
[4] Y. Dong, P. Wen, H. Shi, Y. Yu, Z. S. Wu, *Adv. Funct. Mater.* **2023**, 34.
[5] S. Zhao, H. Che, S. Chen, H. Tao, J. Liao, X.-Z. Liao, Z.-F. Ma, *Electrochem. Energy Rev.* **2024**, 7.
[6] Z. Huang, P. Jaumaux, B. Sun, X. Guo, D. Zhou, D. Shanmukaraj, M. Armand, T. Rojo, G. Wang, *Electrochem. Energy Rev.* **2023**, 6.
[7] Y. Lu, L. Li, Q. Zhang, Z. Niu, J. Chen, *Joule* **2018**, *2*, 1747.
[8] W. Hou, X. Guo, X. Shen, K. Amine, H. Yu, J. Lu, *Nano Energy* **2018**, *52*, 279.
[9] Y. Yang, S. Yang, X. Xue, X. Zhang, Q. Li, Y. Yao, X. Rui, H. Pan, Y. Yu, *Adv. Mater.* **2024**, *36*, 2308332.
[10] E. Ruoff, S. Kmiec, A. Manthiram, *Adv. Energy Mater.* **2024**, *14*, 2402091.
[11] L. Zhou, J. D. Bazak, C. Li, L. F. Nazar, *ACS Energy Lett.* **2024**, *9*, 4093.
[12] P. Ridley, L. H. B. Nguyen, E. Sebti, B. Han, G. Duong, Y.-T. Chen, B. Sayahpour, A. Cronk, G. Deysher, S.-Y. Ham, J. A. S. oh, E. A. Wu, D. H. S. Tan, J.-M. Doux, R. Cle´ment, J. Jang, Y. S. Meng, *Matter* **2024**, *7*, 485.
[13] J. Park, J. P. Son, W. Ko, J.-S. Kim, Y. Choi, H. Kim, H. Kwak, D.-H. Seo, J. Kim, Y. S. Jung, *ACS Energy Lett.* **2022**, *7*, 3293.
[14] H. Kwak, J. Lyoo, J. Park, Y. Han, R. Asakura, A. Remhof, C. Battaglia, H. Kim, S.-T. Hong, Y. S. Jung, *Energy Storage Mater.* **2021**, *37*, 47.

© 2025 The Author(s). Advanced Functional Materials published by Wiley-VCH GmbH

16163028, 2026, 8, Downloaded from https://advanced.onlinelibrary.wiley.com/doi/10.1002/adfm.202516657 by Forschungszentrum Jülich GmbH Research Center, Wiley Online Library on [28/01/2026]. See the Terms and Conditions (https://onlinelibrary.wiley.com/terms-and-conditions) on Wiley Online Library for rules of use; OA articles are governed by the applicable Creative Commons License

[15] E. A. Wu, S. Banerjee, H. Tang, P. M. Richardson, J. M. Doux, J. Qi, Z. Zhu, A. Grenier, Y. Li, E. Zhao, G. Deysher, E. Sebti, H. Nguyen, R. Stephens, G. Verbist, K. W. Chapman, R. J. Clement, A. Banerjee, Y. S. Meng, S. P. Ong, *Nature Communnications* **2021**, *12*, 1256.
[16] X. Lin, S. Zhang, M. Yang, B. Xiao, Y. Zhao, J. Luo, J. Fu, C. Wang, X. Li, W. Li, F. Yang, H. Duan, J. Liang, B. Fu, H. Abdolvand, J. Guo, G. King, X. Sun, *Nat. Mater.* **2025**, *24*, 83.
[17] S. Zhang, F. Zhao, J. Chen, J. Fu, J. Luo, S. H. Alahakoon, L.-Y. Chang, R. Feng, M. Shakouri, J. Liang, Y. Zhao, X. Li, L. He, Y. Huang, T.-K. Sham, X. Sun, *Nat. Commun.* **2023**, *14*, 3780.
[18] G. Jia, Z. Deng, D. Ni, Z. Ji, D. Chen, X. Zhang, T. Wang, S. Li, Y. Zhao, *Frontiers in Chemistry* **2022**, *10*, 952875.
[19] S. Wang, Q. Bai, A. M. Nolan, Y. Liu, S. Gong, Q. Sun, Y. Mo, *Angew. Chem., Int. Ed.* **2019**, *58*, 8039.
[20] P.-J. Lian, B.-S. Zhao, L.-Q. Zhang, N. Xu, M.-T. Wu, X.-P. Gao, *J. Mater. Chem. A* **2019**, *7*, 20540.
[21] A. Salyulev, E. Vovkotrub, *Russ. J. Appl. Chem.* **2013**, *86*, 687.
[22] B. Zheng, Z. Wang, F. Qi, X. Wang, B. Yu, W. Zhang, Y. Chen, *Appl. Surf. Sci.* **2018**, *435*, 563.
[23] J. Ibáñez, T. Woźniak, F. Dybala, R. Oliva, S. Hernández, R. Kudrawiec, *Sci. Rep.* **2018**, *8*, 12757.
[24] P. Wei, Y. Yang, C. J. Liu, H. Y. Gao, *Adv. Funct. Mater.* **2024**, *34*, 2409769.
[25] D. Wang, X. Zhang, G. Guo, S. Gao, X. Li, J. Meng, Z. Yin, H. Liu, M. Gao, L. Cheng, *Adv. Mater.* **2018**, *30*, 1803285.
[26] L. Fu, F. Wang, B. Wu, N. Wu, W. Huang, H. Wang, C. Jin, L. Zhuang, J. He, L. Fu, Y. Liu, *Adv. Mater.* **2017**, *29*, 1700439.
[27] S. Ivanova, E. Zhecheva, R. Kukeva, D. Nihtianova, L. Mihaylov, G. Atanasova, R. Stoyanova, *ACS Applied Materials Interfaces* **2016**, *8*, 17321.
[28] C. Wagner, A. Naumkin, A. Kraut-Vass, J. Allison, C. Powell, J. Rumble Jr., NIST standard reference database 20, version 3.4 (web version), National Institute of Standards Technology, Gaithersburg, MD, **2003**, 20899.
[29] I. Bello, W. Chang, W. Lau, *J. Appl. Phys.* **1994**, *75*, 3092.
[30] M. Ismail, Y. Zhao, X. Yu, S. Dou, *Energy Education Science and Technology Part A: Energy Science and Research* **2012**, *30*, 107.
[31] Q. Wang, J. Zhao, X. Wang, *The Journal of Physical Chemistry A* **2015**, *119*, 2244.
[32] E. Sebti, J. Qi, P. M. Richardson, P. Ridley, E. A. Wu, S. Banerjee, R. Giovine, A. Cronk, S.-Y. Ham, Y. S. Meng, S. P. Ong, R. J. Clément, *J. Mater. Chem. A* **2022**, *10*, 21565.
[33] M. Wilkening, P. Heitjans, *ChemPhysChem* **2012**, *13*, 53.
[34] P. Heitjans, M. Wilkening, *MRS Bull.* **2009**, *34*, 915.
[35] Z. L. Dong, Y. Gan, V. Martins, X. Wang, B. Fu, E. Jin, Y. Gao, Y. Hu, X. Lin, Y. Yuan, C. Turner, X. Pang, H. Abdolvand, Y. Huang, T.-K. Sham, Y. Zhao, *Adv. Mater.* **2025**, *37*, 2503107.
[36] D. Caurant, O. Majérus, E. Fadel, A. Quintas, C. Gervais, T. Charpentier, D. Neuville, *J. Nucl. Mater.* **2010**, *396*, 94.
[37] G. Deysher, Y.-T. Chen, B. Sayahpour, S. W.-H. Lin, S.-Y. Ham, P. Ridley, A. Cronk, E. A. Wu, D. H. Tan, J.-M. Doux, J. A. S. Oh, J. Jang, L. H. B. Nguyen, Y. S. Meng, *ACS Applied Materials Interfaces* **2022**, *14*, 47706.
[38] V. Lacivita, Y. Wang, S.-H. Bo, G. Ceder, *J. Mater. Chem. A* **2019**, *7*, 8144.
[39] Z. L. Dong, Y. Yuan, V. Martins, E. Jin, Y. Gan, X. Lin, Y. Gao, X. Hao, Y. Guan, J. Fu, X. Pang, Y. Huang, Q. H. Tu, T.-K. Sham, Y. Zhao, *Nano Energy* **2024**, *128*, 109871.
[40] X. Chi, Y. Zhang, F. Hao, S. Kmiec, H. Dong, R. Xu, K. Zhao, Q. Ai, T. Terlier, L. Wang, L. Zhao, L. Guo, J. Lou, H. L. Xin, S. W. Martin, Y. Yao, *Nat. Commun.* **2022**, *13*, 2854.
[41] N. Yabuuchi, K. Kubota, M. Dahbi, S. Komaba, *Chem. Rev.* **2014**, *114*, 11636.

© 2025 The Author(s). Advanced Functional Materials published by Wiley-VCH GmbH

16163028, 2026, 8, Downloaded from https://advanced.onlinelibrary.wiley.com/doi/10.1002/adfm.202516657 by Forschungszentrum Jülich GmbH Research Center, Wiley Online Library on [28/01/2026]. See the Terms and Conditions (https://onlinelibrary.wiley.com/terms-and-conditions) on Wiley Online Library for rules of use; OA articles are governed by the applicable Creative Commons License